PAPER

Design and fabrication of integral carbon monoliths combining 3D printing and sol–gel polymerization: effects of the channel morphology on the CO-PROX reaction†

Cristian Yesid Chaparro-Garnica, [iD] Esther Bailón-García, [iD]*
Dolores Lozano-Castelló and Agustín Bueno-López [iD]

A new method to synthesize integral carbon monoliths with a controlled channel morphology has been developed in this work by combining 3D-printing technology and sol–gel polymerization. By this method, robust and consistent carbon monoliths were obtained with a perfect replica of the channel architecture at a microscale range. As a proof of concept, a carbon monolith with tortuous channels that split and join successively along the monolith length has been designed, fabricated and tested as a CuO/CeO_2 support for the preferential oxidation of CO in the presence of H_2 (CO-PrOx), which is a topic of ongoing research for H_2 purification in fuel cells. The behavior of this novel carbon monolith catalyst has been compared with that of a counterpart catalyst prepared with a conventional honeycomb design. Results shown that the wide macroporosity of the carbon network favors the anchoring and dispersion of the active phase both in the channel surface and the carbon network. The channel architecture affects the gas diffusion both through the channel and the carbon network and consequently, affects the active phase accessibility and activity. T_{50} (the temperature to achieve 50% CO conversion) decreases by almost 13 °C at 240 mL min^{-1} in the carbon monolith with tortuous channels (T_{50} = 79.7 °C) compared to the honeycomb monolith (T_{50} = 93.1 °C). The turbulent path created by the tortuous channels favours the active phase–gas contact and even the gas diffusion inside the macropores of the carbon skeleton improving the catalytic performance of the active phase compared to that by the conventional honeycomb design. Thus, this work demonstrates the potential of 3D printing to improve the catalytic supports currently available.

1. Introduction

Ceramic monoliths with a cellular structure are widely used as catalytic supports in several industrial applications, such as selective catalytic NO_x reduction (SCR) systems of thermal power plants or three-way catalysts installed in automobiles.[1] These materials stand out for their high mechanical strength, low pressure drop, thermal stability and versatility in use (easy cleaning, replacement, *etc.*). However, in this type of ceramic material, the surface characteristics (porosity and surface chemistry) cannot be widely modified and tailored. In that sense, carbon materials have interesting properties which make them appropriate candidates for a wide range of applications, such as adsorption, gas separation or chemical

reactions, either as catalysts or as catalyst supports.[2] The high surface area and pore volume, the stability in acidic and basic environments, and the flexibility that carbon materials have to tailor both its textural properties and chemical characteristics make carbon a very versatile material. Thus, cellular carbon monoliths have been proposed for several applications.[3,4]

Two types of carbon-based cellular monoliths can be distinguished: carbon-coated ceramic monoliths and integral carbon monoliths.[5]

Carbon-coated ceramic monoliths usually present higher mechanical resistance, which is provided by the ceramic template. However, integral carbon cellular monoliths have higher surface areas per total weight (or volume) which are preferred in some applications. Carbon-coated monoliths are prepared using a ceramic monolith (cordierite, mullite, alumina or clays) on which a carbon layer is well-adhered by dip-coating the monolith in an organic resin followed by a subsequent carbonization process[5–8] or by chemical vapor deposition of hydrocarbons onto the ceramic monolith.[9–11]

Departamento de Química Inorgánica, Universidad de Alicante, Carretera de San Vicente del Raspeig s/n, E03080, Alicante, Spain. E-mail: estherbg@ugr.es

Catalysis Science & Technology

Integral cellular monoliths are synthesized using a paste composed of a carbon material or precursor, binders and organic or inorganic fillers. This paste is extruded, dried and finally carbonized to obtain the cellular carbon monolith. The use of binders affects the porosity of carbon materials[12] and obvious shrinkage is observed after the carbonization which are both important drawbacks. To avoid this shrinkage, the carbon material can be used in combination with ceramic binders to achieve enough strength and stability.[13–15]

Regardless of the strategy used to prepare carbon monoliths, the channel morphology is restricted to straight and not complex designs due to the manufacturing technology employed, commonly extrusion. Advanced designs could provide an important breakthrough in catalysis since a better use of normally expensive active phases can be achieved. Conventional honeycomb monoliths force a laminar fluid flow through its straight channels, which induces radial mass transfer limitations and thus, an unfavorable active phase–reagent contact with the consequent loss of activity. In that sense, advanced channel designs, *e.g.* tortuous channels, can induce turbulence inside the channel favoring the active phase-reagent interaction that enhances the catalytic performance. Nevertheless, advanced designs cannot be obtained with the technology available to date decreasing the versatility of the use of cellular monoliths in catalysis.

The rise and development of 3D printing technology in the last years provide a new tool for designing monoliths with desired morphologies. However, most of the attempts are focused on the development of polymeric–ceramic hybrid filaments[16–21] or inks[22–25] to be fused or extruded in conventional fused deposition modeling (FDM) or direct ink writing (DIW) printers. However, the polymeric matrix limits the application of these 3D printed monoliths in many catalytic reactions due to the poor thermal and chemical stability. Most of the studies conducted to date are focused on the incorporation of active phases to polymer-based 3D printed monoliths but always results in honeycomb monoliths, losing sight to the morphology design and therefore, the possibilities that the 3D printing could entails in catalysis has not been really explored.

Thus, new strategies must be developed in order to obtain integral carbon monoliths with desired morphologies by using the 3D printing technology. In this manuscript, a new strategy to synthesize integral and pure carbon monoliths with a controlled channel morphology is presented. This procedure combines the versatility of the sol–gel polymerization and the 3D printing technology and thus, advanced and complex designs could be possible. As a proof of concept, two different channel architectures were designed and printed, and their effect on the catalytic performance of the CuO/CeO$_2$ active phase in the preferential oxidation of CO (CO-PrOx), which is a topic of ongoing research for H$_2$ purification in fuel cells, was analyzed.

2. Experimental

2.1. Catalyst preparation

Active phase synthesis. CeO$_2$ was synthesized by calcination of cerium nitrate hexahydrate (Ce(NO$_3$)$_3$·6H$_2$O, 99.5% from Alfa Aesar) in a muffle at 500 °C for 4 h.

The CuO/CeO$_2$ active phase was prepared by incipient wetness impregnation of the previously synthesized CeO$_2$ with a suitable amount of Cu(NO$_3$)$_2$·2.5H$_2$O (≥98% from Sigma-Aldrich) to obtain 5 wt% Cu. Then, the impregnated CeO$_2$ was introduced into a preheated muffle at 200 °C to flash dry and finally, treated at 400 °C for 2 h at a heating rate of 2 °C min^{-1} to decompose the CuO precursor salt and to obtain the final CuO/CeO$_2$ active phase.

Monolithic support preparation. The carbon monoliths were prepared by sol–gel polymerization of resorcinol (R) and formaldehyde (F) in the presence of a 3D-printed polymeric template which provides the desired channel architecture. The polymeric template was printed with two designs: a conventional honeycomb design (CD, Fig. 1a) composed of straight channels and a tortuous design (TD, Fig. 1b) with channels that split and join successively along the monolith length to create a tortuous path. Copolyester (CPE+ supplied by Ultimaker) was selected as the polymer to print the templates, and other polymers failed (PLA, ABS and PC) because they negatively affected the polymerization of the R–F mixture. The templates were printed using an Ultimaker 2+ 3D printer. Once the template was prepared, it was introduced in a glass tube and the tube was filled with a
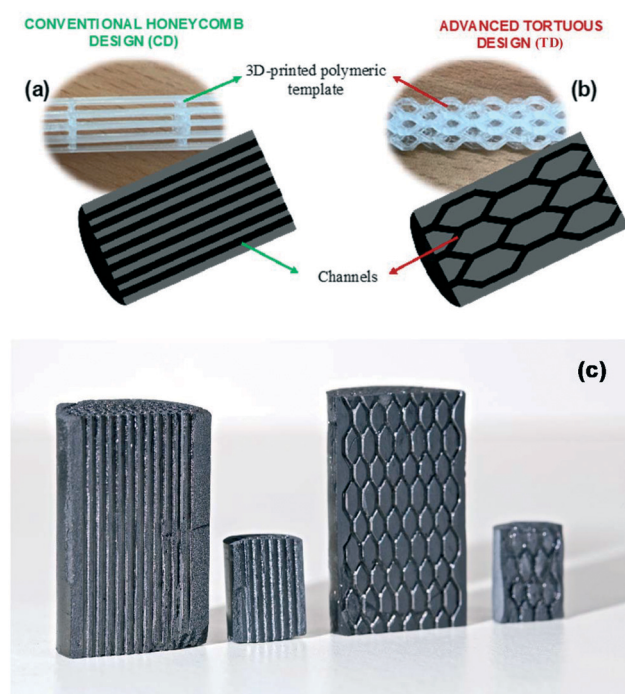

Fig. 1 3D printed templates: a) conventional honeycomb channel design (CD) and b) advanced tortuous channel design (TD). (c) Picture of the carbon monoliths (the small monoliths with a 1 cm diameter have been used to prepare the supported catalysts used in this study).

This journal is © The Royal Society of Chemistry 2021

Catal. Sci. Technol., 2021, **11**, 6490–6497 | **6491**

resorcinol, formaldehyde and water mixture (R/F and R/W molar ratios were 1/2 and 1/15, respectively). Then, the tube was sealed and subjected to polymerization and thermal aging for 1 day at room temperature, 1 day at 50 °C and 5 days at 80 °C. The organic gel was unmolded, cut to the desired length, and introduced in acetone (3 days, changing acetone twice daily) to exchange the water within the pores with acetone and to favour the drying process. Finally, the organic monoliths were dried at room temperature for 3 days and at 50 °C overnight and carbonized at 900 °C for 2 h at a heating rate of 1 °C min^{-1}. The final carbon monoliths have a dimension of 1 cm diameter × 1.7 cm length. Fig. 1c shows a picture of the carbon monoliths prepared in this study, including the 1 cm monoliths used for the further preparation of the supported catalysts and the larger monoliths prepared to analyze the eventual scaling up of the synthesis process.

Active-phase loading into the 3D-printed monoliths. The previously synthesized CuO/CeO_2 active phase was loaded on the 1 cm carbon monoliths by dip-coating the monoliths into a CuO/CeO_2 ethanolic suspension (15% wt). Then, the impregnated monoliths were dried for 24 h at room temperature, rotating horizontally to obtain adequate dispersion, and subsequently treated at 250 °C in static air for 24 h at a heating rate of 4 °C min^{-1}. Finally, the excess of the active phase that can obstruct the channels and that is not adhered to the support was eliminated by means of compressed air. The amount of the active phase incorporated in both monoliths was 110 ± 5 mg (0.17 g active phase per g of monolith).

2.2. Catalyst characterization

The loading of the active phase anchored in the carbon monoliths was analyzed by gravimetric measurements after burning the supported catalysts at 700 °C for 2 h.

Thermogravimetric analysis was performed to determine the thermal stability of the carbon-based catalysts using SDT 2960 DSC-TGA equipment. The temperature was raised up to 900 °C at 10 °C min^{-1} under air flow.

Gas adsorption measurements (N_2 at −196 °C) were performed using Quantachrome Autosorb-6B equipment to obtain information about the surface area of the powder catalyst. The samples were degassed at 110 °C for 8 h before the gas adsorption measurements. Hg porosimetry was carried out on a Poremaster 60 GT (Quantachrome) using the catalysts previously outgassed at 50 °C under vacuum for 12 h.

The active phase distribution on the carbon monoliths was analyzed by scanning electron microscopy (SEM) using an S-3000 N microscope from HITACHI equipped with an XFlash 3001 X-ray detector from Bruker for microanalysis (EDS) and chemical mapping.

2.3. Catalytic tests

The catalytic performance of the monolithic catalysts was analyzed in the preferential oxidation of CO. The monolithic catalyst was fixed in a stainless-steel cylindrical reactor. The

outflow gases were analyzed using a gas chromatograph (Agilent Technologies 6890 N) equipped with two columns: Porapak Q 80/100 for CO_2 and H_2O separation and Molecular Sieve 13X for O_2 and CO separation.

In a typical experiment, the reaction gas mixture (2% CO, 2% O_2, and 30% H_2 balanced in He) was fed to the reactor at room temperature for 30 min, and then the temperature was raised until 250 °C at 2 °C min^{-1}. Then, the reaction gas mixture was replaced with 5% O_2 in He. The gas mixture density estimated is 0.133 kg m^{-3} and its viscosity is 0.0186 cP. After 15 min at 250 °C, the furnace was switched off, the reactor was cooled down in O_2/He without controlling the cooling rate, and a new test was performed following the same protocol. After confirming that the catalyst is stable in consecutive runs, experiments were performed with total flows of 150, 180, 240 and 300 mL min^{-1}. The CO conversion and selectivity to CO were calculated.

3. Results and discussion

3.1. Characterization of the CuO/CeO_2/carbon monolith catalysts

Fig. 2 shows the images of the organic and carbon monoliths with both channel designs. It is observed that regardless of the design used, the R–F mixture is successfully polymerized in all the free spaces left by the polymeric template (Fig. 2a, above and below). Free spaces are not observed neither in the organic gel walls nor in the organic gel–template interface indicating good wettability and affinity between the polymeric template and the R–F mixture. Consistent and robust carbon monoliths were obtained after carbonation (Fig. 2b), and Fig. 2c shows that the template was removed and the channels were opened. A perfect replica of the template was obtained without any breakage in the carbon walls was observed for both channel architectures.
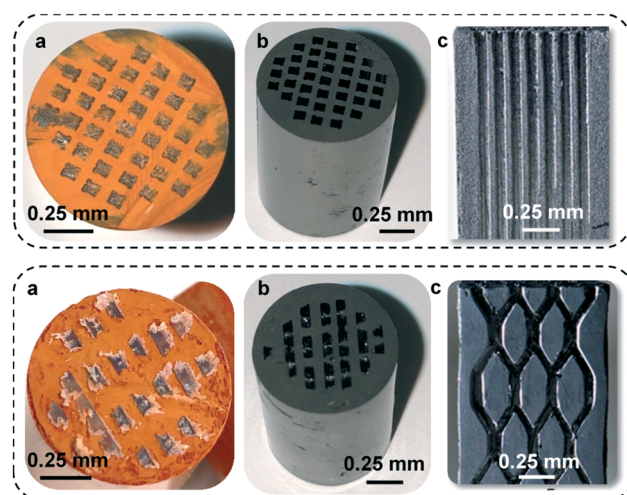

Fig. 2 Images of the organic (a) and (b and c) 1 cm diameter carbon monoliths. General views (a and b) and transverse section (c). Above: the conventional design (CD) and below: the tortuous design (TD).
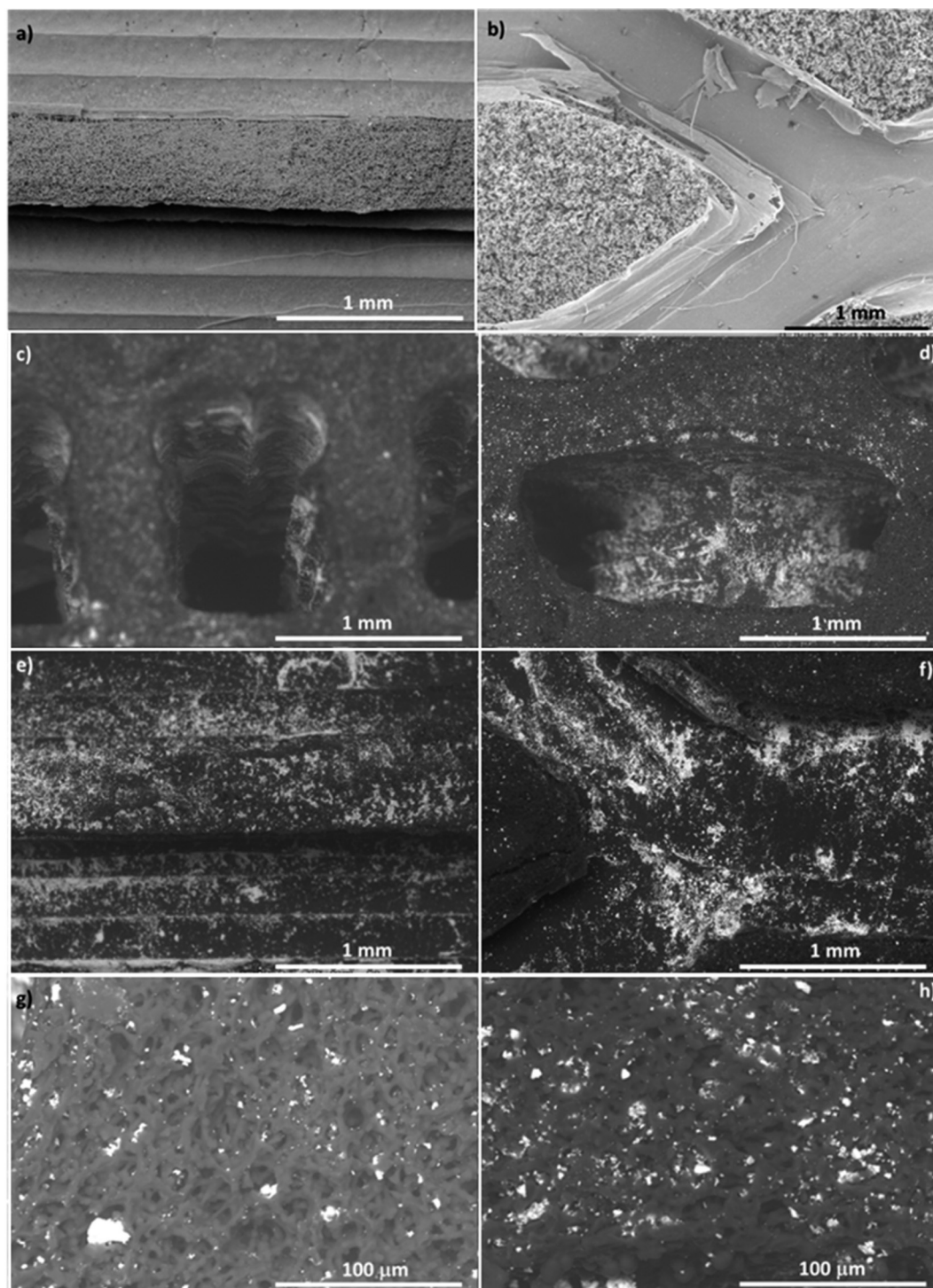
6492 | *Catal. Sci. Technol.*, 2021, **11**, 6490–6497

This journal is © The Royal Society of Chemistry 2021

Fig. 3 SEM images of a and b) the carbon monoliths and c–h) CuO/CeO$_2$-supported catalysts: conventional design (left) and tortuous design (right). c) and d) Channel entrance, e) and f) transverse section of the monoliths and g) and h) carbon wall.

This perfect replica was corroborated by SEM (Fig. 3a and b). Note that the channel walls are not completely flat and smooth, but lines of 0.2 mm width are observed which is explained based on the FDM 3D-printing process. The 3D-printed architectures are obtained by the layer-by-layer deposition of a fused polymer; thus, each plane is formed by several lines of the polymer. Therefore, even the printing

details at the microscale are perfectly reproduced, which means that the accuracy of the replica achieved with this sol–gel polymerization process reaches the micrometer range.

The CuO/CeO$_2$ active phase was deposited in both the monoliths by dip-coating and its dispersion was analyzed by SEM (Fig. 3c–h). The amount of the active phase incorporated in both the monoliths was quite similar (110 ± 5 mg) and, as

observed by SEM, it was homogeneously dispersed along all the carbon monolith. Note that the carbon walls (Fig. 3g and h) are formed by fused primary particles forming a coral structure that left very wide pores (several tens of μm). This large porosity was corroborated by N_2-adsorption and Hg porosimetry (Fig. 4a and b, respectively). Low N_2-adsorption is observed, denoting a low volume of micro and mesopores, whereas a high volume of wide macropores (4–50 μm) is obtained by Hg-porosimetry ($V_{4-50} = 1.07$ cm^3 g^{-1}). This large porosity favors the diffusion of the ethanolic CuO/CeO$_2$ dispersion inside the entire monolith during the dip-coating process and thus, the active phase is homogeneously distributed both in the channel and inside the carbon wall (Fig. 3e–h), enhancing the active phase incorporation and distribution along the carbon monolith unlike other ceramic or polymeric monoliths.

The powdered and supported CuO/CeO$_2$ active phases were characterized by XRD and Raman spectroscopy (Fig. 5) in order to analyse the active phases before and after deposition on the monolith.

The CuO/CeO$_2$ catalyst presents the XRD peaks of the fluorite structure of ceria (Fig. 5a). The CuO peaks are not well-defined indicating the good dispersion of CuO particles on the ceria support. In addition, the CeO$_2$ peaks in the CuO/CeO$_2$ catalyst are slightly displaced in comparison with the CeO$_2$ support indicating a structure distortion of the ceria crystalline structure due to the insertion of Cu^{2+} cations into the ceria lattice. This Cu^{2+} introduction into the ceria lattice was also pointed out by Raman spectroscopy. A displacement of the F$_{2g}$ band was observed for the CuO/CeO$_2$ active phase indicating the introduction of Cu^{2+} cations into the CeO$_2$ lattice (Fig. 5b). A slight shoulder between 500 and 650 cm^{-1} was also detected for the CuO/CeO$_2$ catalyst compared to the CeO$_2$ support, which is related to the presence of oxygen vacancies as a consequence of the incorporation of Cu^{2+} in the fluorite lattice.[26] Similar XRD and Raman patterns were obtained for the powdered and supported CuO/CeO$_2$ active phases indicating that no significant changes in the chemical nature of the active phases were observed after their anchoring on the monolith surface. Note that two new bands at 1332 and 1599 cm^{-1} are identified in the CuO/CeO$_2$ active phase supported on the carbon monolith assigned to D and G carbon bands.[27] Overall, these results indicate that the
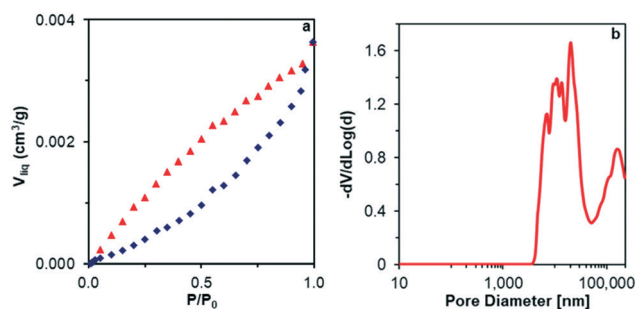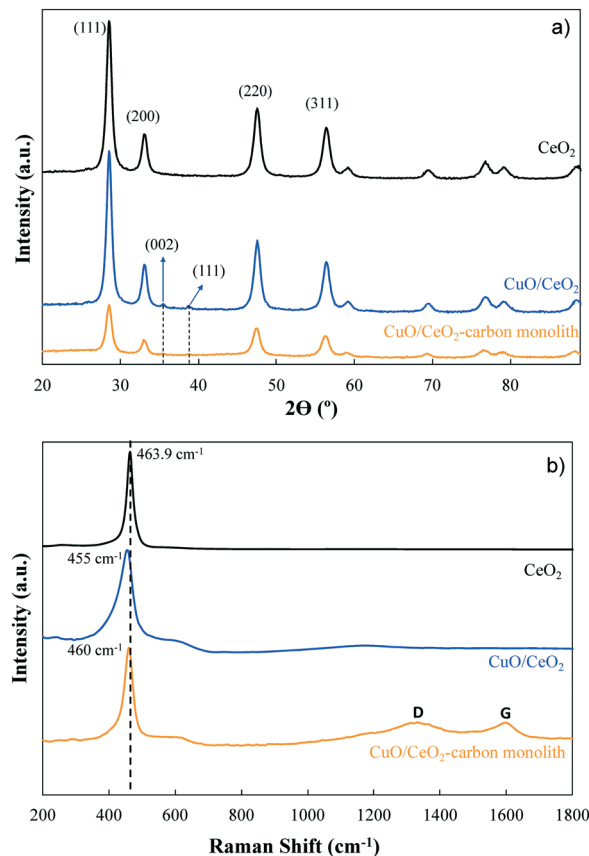

Fig. 5 a) XRD patterns and b) Raman spectra of the CeO$_2$ and CuO/CeO$_2$ catalysts, both powdered and supported (CuO/CeO$_2$–carbon monolith).

deposition process and the interaction with carbon did not affect the chemical nature of the active CuO/CeO$_2$ phase, and therefore, the differences observed in the catalytic performance are related to the design of the monoliths and not due to induced modifications to the active phase during the deposition process.

On the other hand, the thermal stability of carbon monoliths is critical in catalysis. The stability of the carbon monoliths in inert or reducing atmospheres is ensured, however, the stability in oxidizing atmospheres must be analyzed. Thus, the thermal stability of the carbon support and CuO/CeO$_2$-supported carbon catalyst in an oxidizing atmosphere was analyzed by thermogravimetric analysis in air flow (Fig. 6). Carbon monoliths start to burn at a temperature of 550 °C. This temperature is decreased to 490 °C by the deposition of the CuO/CeO$_2$ active phase due to the well-known role of ceria as a combustion catalyst. However, this temperature is high enough to allow the use of these carbon monoliths in a wide range of catalytic reactions.

Fig. 4 Characterization of the textural properties of the CD carbon monolith. a) N_2-adsorption isotherm and b) Hg-porosimetry.

3.2. Catalytic tests: CO oxidation under CO-PrOx conditions

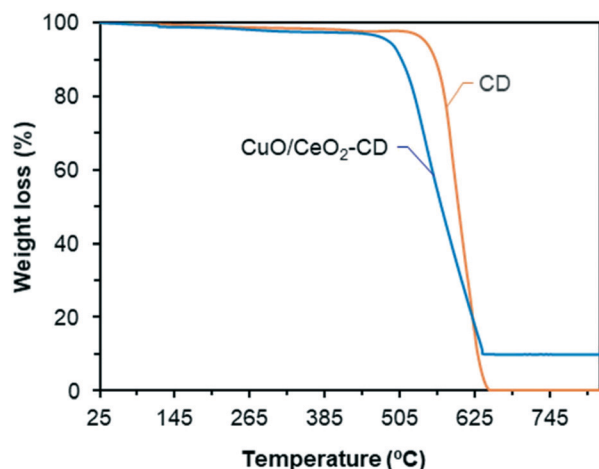The catalytic performance of the CuO/CeO$_2$-supported carbon monoliths was studied in the oxidation of CO under CO-PrOx

Fig. 6 Thermogravimetric analysis results in air of pure and CuO/CeO$_2$-supported carbon monoliths (CD: the carbon monolith with the conventional design; CuO/CeO$_2$-CD: CuO/CeO$_2$ loaded on the carbon monolith with the conventional design).

conditions (2% CO, 2% O$_2$, and 30% H$_2$ in He balance) under flows ranging from 90 to 300 mL min^{-1}. The CO conversion
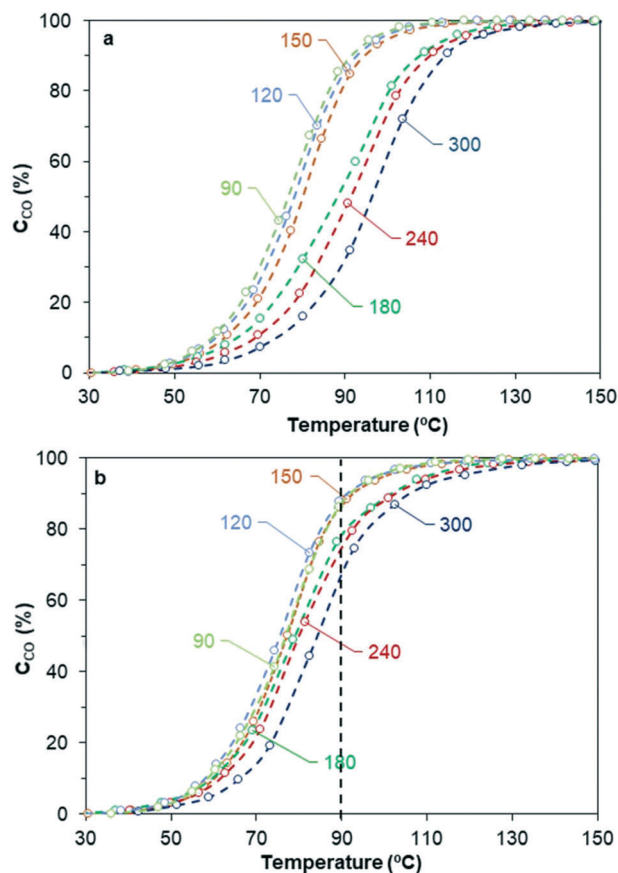

Fig. 7 Conversion of CO (C_{CO}) over the CuO/CeO$_2$ active phase supported on the carbon monolith with a) the conventional design (CD) and b) tortuous design (TD) for CO oxidation under CO-PrOx conditions: 2% CO, 2% O$_2$, and 30% H$_2$ in He balance at flows ranging from 90 to 300 mL min^{-1}.

at different flows over both monolithic catalysts is depicted in Fig. 7a and b. As expected, the CuO/CeO$_2$ active phase is very active (the total conversion is obtained at temperatures below 130 °C) and very selective (Fig. S1†) to the CO-PrOx reaction. However, the effect of the flow is very different depending on the channel design. For both designs, at low flow rates (90–150 mL min^{-1}), changes in the flow did not highly affect the conversion. However, at flows higher than 150 mL min^{-1}, the conversion decreased for both carbon monoliths, and this decrease is more severe for the conventional honeycomb design. This seems to indicate that the active phase is used in different ways depending on the flow and the channel design. At low flows, only a slight improvement in the conversion is obtained with the tortuous channel design compared to the conventional one, which indicates that the active phase–gas contact is similar and independent of the channel configuration. However, at high flows, the tortuous path improved the conversion because it improves the CuO/CeO$_2$–gas contact.

As it was pointed out in the previous section, a large porosity is obtained in the carbon monoliths and so, the active phase is distributed both in the channels and inside the carbon skeleton. At low flow rates (90–150 mL min^{-1}), the gas can easily circulate through both the channels and the wide pores of the carbon skeleton in both monoliths, which minimizes the effect of the imposed laminar gas circulation inside the channels of the conventional honeycomb design. However, by increasing the flow rate (>150 mL min^{-1}), most of the gas is imposed to flow through the channels and thus, the activity decreased due to the loss of the active phase accessible to the gases (Fig. 8, right). This decrease is less severe in the monolith with the tortuous design because the turbulent path created by the tortuous channels favours the active phase–gas contact and even the gas diffusion inside the macropores of the carbon skeleton (Fig. 8, left).

To analyse in more detail the effect of mass diffusion on the reaction rate, the CO conversion rate normalized by the weight of CuO/CeO$_2$ was calculated and the results are shown
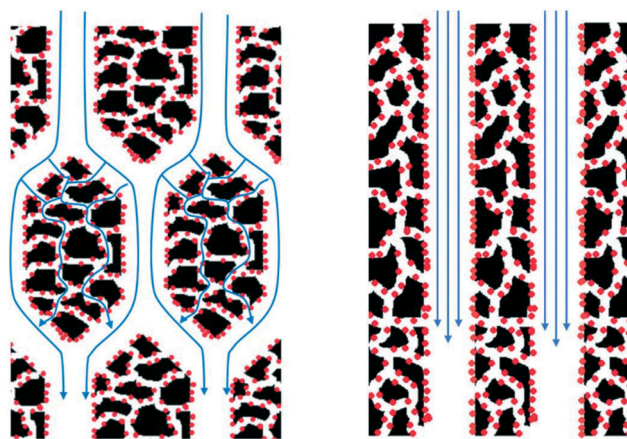

Fig. 8 Gas diffusion on the carbon monoliths at high flow rates (>150 mL min^{-1}). CuO/CeO$_2$ (•).

This journal is © The Royal Society of Chemistry 2021

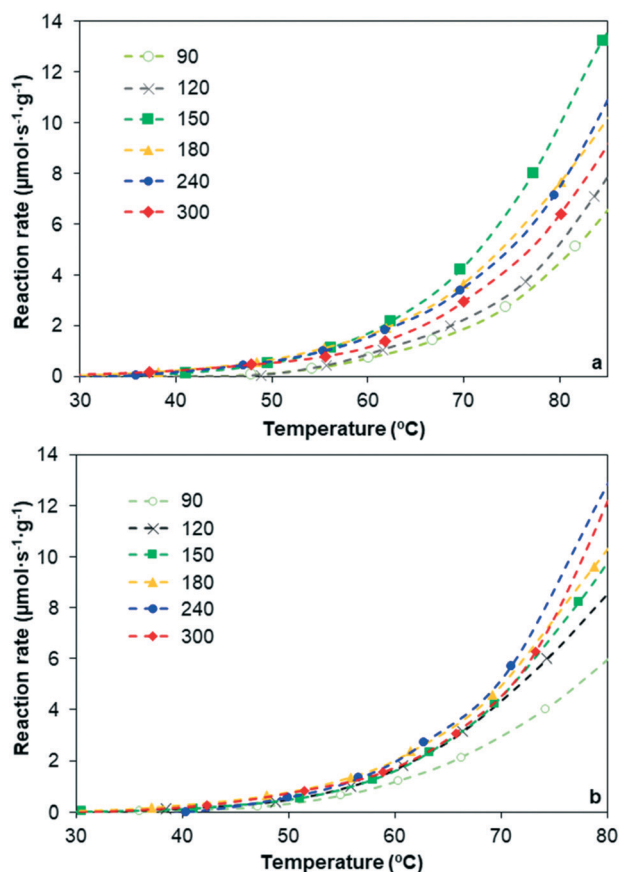*Catal. Sci. Technol.*, 2021, **11**, 6490–6497 | **6495**

Fig. 9 CO conversion rates normalized by the weight of CuO/CeO$_2$ over the catalysts supported on the carbon monoliths with a) the conventional design and b) advanced tortuous design at several gas flow rates (90–300 mL min^{-1}).
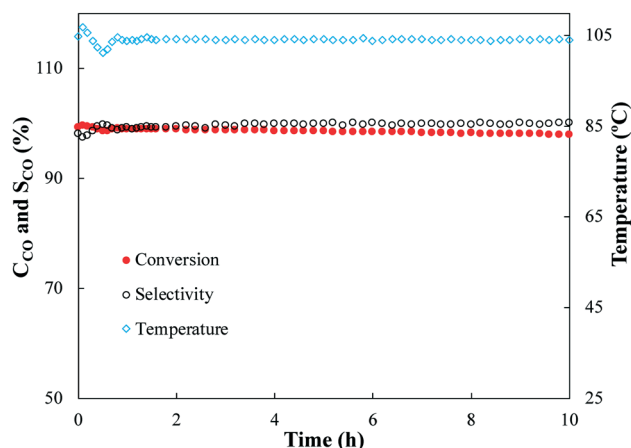

Fig. 10 CO conversion (C_{CO}) and selectivity to CO (S_{CO}) (in the main axis) and temperature (in the secondary axis) over the CuO/CeO$_2$ supported on the carbon monolith with the advanced tortuous design. Reaction conditions: 2% O$_2$, 2% CO, 30% H$_2$, and He balance. A total flow of 150 mL min^{-1} at a constant temperature (104 °C).

in Fig. 9. A heterogeneous catalytic reaction can be controlled by two main steps: the diffusion of reagents and products from/to the fluid bulk to/from the catalyst surface or the chemical reaction.[28,29] In the former (diffusion control of the reaction rate), the reaction rate depends on the gas flow and consequently, on the design of the monolith, whereas in the latter (chemical control of the reaction rate), the reaction rate depends on the effectiveness of the active phase of the catalyst. Fig. 9 shows that the monolith with the conventional channel design is always under diffusion control, whereas the monoliths with the tortuous design at flows higher than 90 mL min^{-1} are under chemical control, at least up to 70 °C. This indicates that the existence of more tortuous channels in the monolith improves the availability of active sites to carry out the chemical reaction. Under diffusional control regime, the increase of the volumetric flows favours the rapid supply of reactants and simultaneously withdrawing the products, favouring the chemical reaction rate. In the case of the conventional honeycomb carbon monolith, which is always under diffusion control, this improvement of the chemical reaction rate occurs with the increase of the flow from 120 mL min^{-1} to 150 mL min^{-1} above which the reaction rate decreases by increasing the flow. This reaction

rate decrease by increasing the flow can be ascribed, as it has previously been commented, to the imposed flow through the straight channels and thus, the loss of the active phase accessible for catalytic reactions (Fig. 8, right). In the case of the monolith with tortuous channels, the tortuous path favours the diffusion of gas inside the pores of the carbon skeleton enhancing the catalytic reaction rate (Fig. 8, left).

Finally, an isothermal catalytic test was performed at 104 °C for a long time (10 h) with the carbon-based monolithic catalyst, in order to analyse the stability. The results in Fig. 10 show that both the CO conversion (98%) and CO selectivity (99%) remain almost constant or even increase during the whole experiment indicating that this catalyst is very stable for a long reaction time. The catalyst was also characterized after the stability test and textural and chemical modifications were not observed after and before the reaction (Fig. S2 and S3†).

Thus, this work demonstrates the potential of 3D printing to improve the conventional catalytic honeycomb supports, which allows obtaining higher conversion with the same amount of active phase.

Conclusions

A new strategy to synthesize integral carbon monoliths is presented in this work, which combines 3D-printing and sol–gel technologies.

A 3D polymer printer was used to generate molds with different geometries of channels that are then filled with the carbon gel precursor solution, subjected to a controlled polymerization, gelation and curing process and finally dried and carbonized. SEM images showed that an accurate replica of the channel architecture is obtained during polymerization, which reaches the micrometer range.

Monoliths with two different channel morphologies were synthesized: a conventional honeycomb design composed of

6496 | *Catal. Sci. Technol.*, 2021, **11**, 6490–6497

This journal is © The Royal Society of Chemistry 2021

straight channels and an advanced tortuous design with channels that split and join successively along the monolith length to create a tortuous path.

The effect of the channel architecture was analyzed in the CO-PrOx reaction using CuO/CeO_2 as the active phase. The large porosity obtained in the carbon network favors the dispersion and anchoring of the CuO/CeO_2 active phase both in the channel surface and the carbon wall. However, the gas diffusion in the entire monolith, and thus the accessibility to the active sites and its activity, is affected by the channel design. In the tortuous design, the turbulent path created a favorable active phase–gas contact, enhanced the rapid mass transfer toward and from the active sites to the gas bulk and even, the gas diffusion inside the macropores of the carbon skeleton improving the catalytic performance in comparison with the conventional honeycomb monolith.

This work demonstrates the potential of 3D printing in the design of monoliths with a non-conventional honeycomb structure for catalytic applications.

Conflicts of interest

There are no conflicts to declare.

Acknowledgements

References

1 J. L. Williams, *Catal. Today*, 2001, **69**, 3–9.
2 E. Pérez-Mayoral, V. Calvino-Casilda and E. Soriano, *Catal. Sci. Technol.*, 2016, **6**, 1265–1291.
3 M. Ouzzine, G. A. Cifredo, J. M. Gatica, S. Harti, T. Chafik and H. Vidal, *Appl. Catal., A*, 2008, **342**, 150–158.
4 L. Liu, Z. Liu, J. Yang, Z. Huang and Z. Liu, *Carbon*, 2007, **45**, 2836–2842.
5 C. Moreno-Castilla and A. F. Pérez-Cadenas, *Materials*, 2010, **3**, 1203–1227.
6 A. F. Pérez-Cadenas, M. M. P. Zieverink, F. Kapteijn and J. A. Moulijn, *Catal. Today*, 2005, **105**, 623–628.
7 J. Singh, H. Bhunia and S. Basu, *J. Taiwan Inst. Chem. Eng.*, 2018, **89**, 140–150.
8 T. Valdés-Solís, G. Marbán and A. B. Fuertes, *Microporous Mesoporous Mater.*, 2001, **43**, 113–126.
9 S. Morales-Torres, A. F. Pérez-Cadenas, F. Kapteijn, F. Carrasco-Marín, F. J. Maldonado-Hódar and J. A. Moulijn, *Appl. Catal., B*, 2009, **89**, 411–419.
10 E. García-Bordejé, I. Kvande, D. Chen and M. Rønning, *Carbon*, 2007, **45**, 1828–1838.
11 E. García-Bordejé, I. Kvande, D. Chen and M. Rønning, *Adv. Mater.*, 2006, **18**, 1589–1592.
12 D. P. Vargas, L. Giraldo and J. C. Moreno-Piraján, *Int. J. Mol. Sci.*, 2012, **13**, 8388–8397.
13 M. Yates, J. Blanco, P. Avila and M. P. Martin, *Microporous Mesoporous Mater.*, 2000, **37**, 201–208.
14 J. M. Gatica, J. M. Rodríguez-Izquierdo, D. Sánchez, C. Ania, J. B. Parra and H. Vidal, *Carbon*, 2004, **42**, 3251–3254.
15 K. P. Gadkaree and M. Jaroniec, *Carbon*, 2000, **38**, 983–993.
16 S. Hwang, E. I. Reyes, K. sik Moon, R. C. Rumpf and N. S. Kim, *J. Electron. Mater.*, 2015, **44**, 771–777.
17 S. H. Masood and W. Q. Song, *Assem. Autom.*, 2005, **25**, 309–315.
18 S. H. Masood and W. Q. Song, *Mater. Des.*, 2004, **25**, 587–594.
19 R. Farrauto, S. Hwang, L. Shore, W. Ruettinger, J. Lampert, T. Giroux, Y. Liu and O. Ilinich, *Annu. Rev. Mater. Res.*, 2003, **33**, 1–27.
20 F. Castles, D. Isakov, A. Lui, Q. Lei, C. E. J. Dancer, Y. Wang, J. M. Janurudin, S. C. Speller, C. R. M. Grovenor and P. S. Grant, *Sci. Rep.*, 2016, **6**, 1–8.
21 Y. Wu, D. Isakov and P. S. Grant, *Materials*, 2017, **10**, 1218.
22 J. Azuaje, C. R. Tubío, L. Escalante, M. Gómez, F. Guitián, A. Coelho, O. Caamaño, A. Gil and E. Sotelo, *Appl. Catal., A*, 2017, **530**, 203–210.
23 J. Lefevere, L. Protasova, S. Mullens and V. Meynen, *Mater. Des.*, 2017, **134**, 331–341.
24 C. R. Tubío, J. Azuaje, L. Escalante, A. Coelho, F. Guitián, E. Sotelo and A. Gil, *J. Catal.*, 2016, **334**, 110–115.
25 J. Zhang, S. Zhao, M. Zhu, Y. Zhu, Y. Zhang, Z. Liu and C. Zhang, *J. Mater. Chem. B*, 2014, **2**, 7583–7595.
26 A. Davó-Quiñonero, M. Navlani-García, D. Lozano-Castelló, A. Bueno-López and J. A. Anderson, *ACS Catal.*, 2016, **6**, 1723–1731.
27 D. B. Schuepfer, F. Badaczewski, J. M. Guerra-Castro, D. M. Hofmann, C. Heiliger, B. Smarsly and P. J. Klar, *Carbon*, 2020, **161**, 359–372.
28 B. Viswanathan, S. Sivasanker and A. Ramaswamy, *Catalysis, principles and application*, Narosa Publishing House, New Delhi, 2002.
29 I. Chorkendorff and J. W. Niemantsverdriet, *Concepts of Modern Catalysis and Kinetics*, Wiley-VCH, Weinheim, Germany, 2017.

This journal is © The Royal Society of Chemistry 2021

Catal. Sci. Technol., 2021, **11**, 6490–6497 | **6497**